State of the Art and Future Trends of CFD at NAL (5 March, 2003)
National Aerospace Laboratories, Bangalore; **NAL-SP-0301**, 31–48

RANS Computation of Low Speed Turbulent Flow in Complex Configuration

Sekhar Majumdar, B.N. Rajani, D.S. Kulkarni and Sripathi Mohan

Abstract

An implicit finite volume algorithm based on the numerical solution of Reynolds Averaged Navier stokes (RANS) equation is presented for prediction of incompressible turbulent flow in and around complex configuration. The algorithm uses boundary-conforming, structured grid, collocated variable arrangement with cartesian velocity components as dependent variables, pressure-velocity solution strategy coupled to different low-diffusive discretisation schemes for evaluation of the convective flux at cell faces, first and second order schemes for temporal discrtetisation and the eddy-viscosity based $k - \epsilon$ model with different near wall treatment for turbulence simulation. Capability and limitation of the algorithm are demonstrated through five different application examples of varied complexities.

1 Introduction

The recent advances of CFD for incompressible flow are gradually proving to be invaluable asset for design and analysis of ship, submarines, underwater missiles, low speed transport aircrafts and a wide variety of equipment design in process industry. Accurate prediction of turbulent flow in or around complex configuration is of great practical interest in the engineering calculation of the overall performance indices of different equipments or processes to be designed. The present paper emphasizes on three important areas of CFD analysis *viz.*, low speed flow, turbulent flow and complex geometry. Flow at low speed, when elastic forces are relatively insignificant, is, in general assumed to be incompressible. For turbulent flow, the understanding of the physics of fluid turbulence is far from complete and the Reynolds Averaged Navier Stokes (RANS) methodology coupled to statistical turbulence models, is often very useful and reliable for computation of statistically stationery turbulent flows. The problem of geometrical complexity, on the other hand, has been addressed by a number of CFD researchers during the last two decades and most of the complexities today can be accurately handled by the use of block-structured, unstructured and overlapping grids.

The present paper first provides an overview of the governing equations, turbulence models and the numerical procedure for a pressure-based time-accurate RANS algorithm for low speed turbulent flows, developed by the authors during the last ten years at the CTFD Division, NAL Bangalore, under the sponsorship of user organizations like DRDO, ISRO and NRB. The capabilities and limitations of the algorithm are thereafter demonstrated through a few application problems.

2 Grid Generation

The computation domain is disecretised for any complex geometry using an algebraic-differential hybrid procedure (Pal et al., 1995; Rajani and Majumdar, 1997), developed recently at NAL by the authors' group to generate structured, boundary-fitted grid with near-orthogonality at the boundaries. This two-step procedure first generates an algebraic grid using a modified Transfinite Interpolation (Soni, 1985) procedure which takes care of the boundary node distribution according to the desired stretching. The grid is thereafter smoothened using an elliptic Poisson solver with control functions derived from the condition of boundary orthogonality.

3 Numerical Solution of RANS Equations

3.1 Momentum and Mass Conservation Equations

The present pressure-based finite volume algorithm uses non-orthogonal curvilinear coordinates with cartesian velocities as dependent variables and the corresponding RANS equations for unsteady turbulent incompressible flow may then be written in a compact form as follows:

Momentum transport for the Cartesian velocity component U_i:

$$\frac{\partial(\rho U_i)}{\partial t} + \frac{1}{J}\frac{\partial}{\partial x_j}\left[(\rho U_i U_k \beta_k^j) - \frac{\mu}{J}\left(\frac{\partial U_i}{\partial x_m}B_m^j + \frac{\partial U_k}{\partial x_m}\beta_i^m \beta_j^k\right) + p\beta_i^j + \rho\overline{u_i u_k}\beta_k^j\right] = S_{U_i} \quad (1)$$

where, J is the transformation Jacobian between cartesian and the curvilinear coordinates, β_j^i and B_j^i are the relevant geometric coefficients related to the transformation, p is the pressure, μ is the fluid viscosity and ρ is the fluid density. j, k and m are used as repeated summing indices along the three grid directions. U_i is the mean Cartesian velocity solved for and $\rho\overline{u_i u_k}$ is the turbulent stress term appearing as correlation between the unknown fluctuating velocity components u_i and u_k, S_{U_i} is any other body forces appearing as source terms. These momentum equations are further supplemented by the mass conservation or the so-called continuity equation which, for incompressible flows, is just a kinematic constraint on the velocity field.

Mass Conservation (Continuity):

$$\frac{\partial}{\partial x_j}\left(\rho U_k \beta_k^j\right) = 0 \quad (2)$$

The turbulent stress terms may be evaluated through some appropriate turbulence models discussed later. In a structured 3D grid environment, a typical control volume is hexahedral defined by the eight cell corners for which the coordinates are determined by an appropriate grid generation method and all the flow variables are stored at the geometric center of each control volume.

3.2 Finite Volume Formulation of Momentum Equations

Integration of the momentum transport equations (Eq. 1) over each control volume transforms the relevant pde's in the form of discrete algebraic equations representing a balance between the convective cum diffusive fluxes through the cell faces and the other remaining terms as volume sources. The convection and diffusion fluxes at the cell faces are computed from the interpolated value of the velocity components and other flow variables and their gradients at the center of six faces of the control volume. The source terms are usually treated to be constant over a control volume and are often linearised ($S_\phi = SU + \phi SP$) for enhancement of numerical stability.

3.2.1 Spatial Discretisation of the Convective Flux

The chosen spatial discretisation scheme basically decides the value or the gradient of the flow variable at the cell faces. Second order accurate Central Difference scheme and two different Upwind schemes *viz.* Central/Upwind Hybrid (Patankar, 1980) and the Quadratic Upwind scheme QUICK (Leonard, 1979) have been formulated, assessed for their relative performance and used in the present algorithm. The detailed algebra of the schemes are discussed in other reports (Kulkarni et al., 2001). The numerical instabilities are avoided using a deferred correction procedure (Khosla and Rubin, 1974). In this procedure, a suitable weighting function is used to blend the flux from the desired scheme with upwind fluxes which allows some small numerical diffusion but ensures numerical stability of the solution.

3.2.2 Temporal Discretisation of the Unsteady Term

The time derivative appearing in the momentum equations is discretised, either using the 1^{st} order accurate, two level Euler backward scheme $\dfrac{\partial \phi}{\partial t} = \dfrac{\phi^{(n+1)} - \phi^n}{\Delta t}$ or the 2^{nd} order accurate three-level fully implicit scheme. $\dfrac{\partial \phi}{\partial t} = \dfrac{1.5\phi^{n+1} + 0.5\phi^{(n-1)} - 2\phi^n}{\Delta t}$

3.2.3 Flux Balance Equation

Using suitable metric coefficients β_i^j of the geometric transformation, derived in the form of projection areas of the cell faces, appropriate discretisation of convective and unsteady terms and the linearisation of the source terms S_ϕ, the flux balance equation for any scalar ϕ can be cast into the following quasilinear form:

$$A_P \phi_P^{(n+1)} = \left(\sum A_{nb} \phi_{nb}^{(n+1)} - SU \right) \quad \text{where} \quad A_P = \sum A_{nb} - SP \tag{3}$$

where the coefficient A_{nb} represents the combined effect of convection and diffusion at the six faces of the cell denoted by the suffix nb and SU and SP are the components of the linearised source term S_ϕ. The detailed derivation of Eq. 3 expressing A_{nb} as a function of cell face projection areas, velocity and diffusion coefficient at cell faces and variable values at the cell centre is given in another report (Majumdar et al., 1992).

3.2.4 Pressure Field Computation

The cell centered velocity components U_{iP} are computed from the solution of the momentum equation using a guessed pressure field in the predictor step. In order to avoid the checker-board splitting of velocity and pressure, the principle of Momentum Interpolation (Majumdar, 1988; Peric, 1985) is used to compute the velocity components U_{iw} at the cell faces. In the corrector step, the continuity equation (Eq. 2) is finally transformed to an equation for pressure correction using the momentum equation as a link between the corrections of velocity and pressure. Substitution of the cell-face velocities and their corrections in terms of nodal pressure corrections thus transforms the continuity equation into a linearised algebraic equation of pressure-correction in the same form of Eq.3. Once the pressure correction (p') field is obtained, the pressure field is corrected as $p_{\text{new}} = p_{\text{old}} + \alpha_p p'$, and the corresponding velocity correction are then added to the predicted momentum-satisfying velocities at the cell centers and cell faces so that the cell-wise continuity is also satisfied. The algebraic details of the pressure correction equation is discussed elsewhere (Majumdar et al., 1992).

3.3 Turbulence Model

The task of the turbulence model is to provide a means for calculating the unknown turbulent stresses appearing in the Reynolds-Averaged equations. In the Eddy Viscosity based models, the turbulent stress is expressed in terms of the mean velocity gradients as follows :

$$-\rho\overline{u_i u_j} = \mu_t \left(\frac{\partial U_i}{\partial x_j} + \frac{\partial U_j}{\partial x_i} \right) - \frac{1}{3}\rho\delta_{ij}\overline{u_k u_k} \tag{4}$$

where, U_i is the time-averaged velocity, u_i is the corresponding fluctuating component, ρ is the fluid density, δ_{ij} is the Kronecker Delta and k is the summation index over $k = 1, 2, 3$. The eddy viscosity μ_t is assumed to be an isotropic scalar quantity whose value depends on the local state of turbulence. The present algorithm is provided with two variants of the $k - \epsilon$ turbulence model described in brief in the following subsections.

3.3.1 $k - \epsilon$ Model

According to the eddy viscosity based $k - \epsilon$ model (Launder and Spalding, 1974)μ_t, the turbulent or eddy viscosity is defined as following in terms of the local kinetic energy of turbulence k and its dissipsation, ϵ where

$$k = \frac{1}{2}\overline{u_k u_k} \quad \text{and} \quad \epsilon = \frac{\mu}{\rho}\overline{\beta_k^n \frac{\partial u_k}{\partial x_n} \beta_k^m \frac{\partial u_k}{\partial x_m}} \tag{5}$$

$$\mu_t = \rho C_\mu k^2/\epsilon \tag{6}$$

The spatial distribution of k and ϵ are evaluated solving the transport equations which are also in the same form as of Eq. 1.

k-equation :

$$\frac{\partial(\rho k)}{\partial t} + \frac{1}{J}\frac{\partial}{\partial x_j}\left[(\rho U_j \beta_k^j k) - \frac{(\mu + \mu_t/\sigma_k)}{J}\left(\frac{\partial k}{\partial x_m} B_m^j \right) \right] = P_k - \rho\epsilon \tag{7}$$

ϵ **equation** :

$$\frac{\partial(\rho\epsilon)}{\partial t} + \frac{1}{J}\frac{\partial}{\partial x_j}\left[(\rho U_j \beta_k^j \epsilon) - \frac{(\mu + \mu_t/\sigma_\epsilon)}{J}\left(\frac{\partial \epsilon}{\partial x_m} B_m^j\right)\right] = C_{\epsilon 1}\frac{\epsilon}{k}P_k - C_{\epsilon 2}\rho\frac{\epsilon^2}{k} \tag{8}$$

$$\text{where} \quad P_k = \text{Production of } k = \frac{\mu_t}{J^2}\left(\frac{\partial U_i}{\partial x_n}\beta_j^n + \frac{\partial U_j}{\partial x_m}\beta_j^m\right)\frac{\partial U_i}{\partial x_n}\beta_j^n \tag{9}$$

Closure coefficients: $C_\mu = 0.09, C_{\epsilon 1} = 1.14, C_{\epsilon 2} = 1.92, \sigma_\epsilon = 1.32$

Turbulent mixing is largely suppressed by the proximity of a wall boundary and the $k-\epsilon$ model however does not represent this effect and breaks down below the log layer. The turbulence energy k certainly goes down to zero at the wall but fixing the unknown finite value of the ϵ at wall is however not so obvious. The viscosity-dominated near wall region therefore needs a special treatment. In the present algorithm the near wall zone is treated using either of the following two approaches.

(1) **Wall function approach** : In the Standard Wall Function (Launder and Spalding, 1974) approach, the integration of the flow equations is carried out only up to the first near-wall grid point and the turbulent layer between the first near wall point and the wall is bridged by the logarithmic law of wall. The near wall values of the mean velocity parallel to wall (U) and those of the turbulence scalars (k and ϵ)are as follows:

$$\frac{U}{U_\tau} = \frac{1}{\kappa}\log_e\left(E\frac{yU_\tau}{\nu}\right); \quad k = \frac{U_\tau^2}{C_\mu^{1/2}}; \quad \epsilon = C_\mu^{3/4}\frac{k^{3/2}}{\kappa y} \tag{10}$$

where U_τ = Friction Velocity = $\sqrt{(\text{Wall Shear Stress}, \tau_w/\rho)}$, $E = 0.9$ for smooth wall, Von Karman constant $\kappa = 0.41$ and y = wall normal distance of the first near wall node.

(2) **Damping function approach (Chien, 1982)** : The Low Reynolds number models have been designed to maintain the high Re formulation of the $k-\epsilon$ in the log law region and at the same time tuned through damping functions to fit in the viscous and buffer layers below the log layer. The damping functions f_μ, f_1 and f_2 and the additional terms D and E are introduced in the $k-\epsilon$ equation system to mimic the effect of reduced mixing of the transport rate and the enhancement of turbulence dissipation near the wall.

k**-equation**:

$$\frac{\partial(\rho k)}{\partial t} + \frac{1}{J}\frac{\partial}{\partial x_j}\left[(\rho U_j \beta_k^j k) - \frac{(\mu + \mu_t/\sigma_k)}{J}\left(\frac{\partial k}{\partial x_m} B_m^j\right)\right] = P_k - \rho\tilde{\epsilon} - D \tag{11}$$

ϵ **equation** :

$$\frac{\partial(\rho\tilde{\epsilon})}{\partial t} + \frac{1}{J}\frac{\partial}{\partial x_j}\left[(\rho U_j \beta_k^j \tilde{\epsilon}) - \frac{(\mu + \mu_t/\sigma_\epsilon)}{J}\left(\frac{\partial \tilde{\epsilon}}{\partial x_m} B_m^j\right)\right] = f_1 C_{\epsilon 1}\frac{\tilde{\epsilon}}{k}P_k - f_2 C_{\epsilon 2}\rho\frac{\tilde{\epsilon^2}}{k} - E \tag{12}$$

$$\mu_t = \rho f_\mu C_\mu k^2/\tilde{\epsilon} \tag{13}$$

where,

$$f_\mu = 1 - \exp(-0.0115y^+), \quad f_1 = 1.0, \quad f_2 = 1 - 0.22\exp\left[-\frac{R_t}{6}^2\right] \quad y^+ = \rho\frac{U_\tau y}{\mu}$$

$$R_t = \rho\frac{k^2}{\mu\tilde{\epsilon}}, \quad D = 2\mu\frac{k}{y^2}, \quad E = 2\mu\frac{\tilde{\epsilon}}{y^2}\exp(-0.5y^+), \quad \rho\epsilon = \rho\tilde{\epsilon} + D$$

Stagnation Point Anomaly The $k-\epsilon$ model based on isotropic eddy viscosity concept usually produces an excessive level of k and μ_t near a stagnation point, often encountered in the vicinity of the leading edge of an aerofoil or at the bow end of a naval vessel. An ad-hoc measure has been suggested (Kato and Launder, 1993) to replace the original production term $P_k = 2\mu_t|S|^2$ in the k-transport equation by $P_k = 2\mu_t|S||\Omega|$ where $|S|$ & $|\Omega|$ are the trace of the mean strain rate S and the vorticity tensor Ω respectively. The vorticity usually is low due to almost irrotational bending of the fluid near stagnation zones and hence the calculated values of unrealistic high level of turbulence energy may be avoided.

3.4 Boundary Conditions and Solution Algorithm

At the inlet planes, usually the known boundary values are prescribed. At symmetry or outflow planes, the boundary values are updated using the interior field values so that the appropriate gradient condition is fulfilled. At the wall, the velocity components are set to zero. For near wall zones in turbulent flows, the flow variables are determined by the special near wall treatment used. The boundary pressure values, when required, are extrapolated linearly from the interior field. For periodic/cyclic boundaries, a fictitious control volume is added beyond the physical periodic/cyclic plane and appropriate values of variable and fluxes are transferred from the corresponding interior nodes. The present method uses an iterative decoupled approach and the system of linear equations (Eq.3) is solved for the three velocity components U_i, pressure-correction p' and the other turbulent scalars (k , ϵ) sequentially, using a strongly implicit procedure (Stone, 1968).

3.5 Multiblock Computation Facility

The most critical consideration in any multidomain computation scheme is how to organise the run-time data transfer from one block to the neighbouring one in such a way that the artificially cut boundary interface plane separating any two adjacent blocks is treated exactly like any other interior cell face of the domain in question. Computation is carried out separately for each block and the inter-block influences are effected in the computation through appropriate data transfer facilities. In a parallel computing environment however more than one blocks are clustered in one processor and the interprocessor data transfer after each iteration sweep is effected through standard MPI calls. The NAL parallel machine Flosolver Mk5 has been extensively used for computation of 3D application examples demonstrated later in the paper.

3.6 Multigrid for Convergence Acceleration

The Full Multigrid-Full Approximation Scheme (Mohan and Majumdar, 2002) with the so called V-cycling concept coupled to grid sequencing, has been implemented in the present

algorithm for convergence acceleration. In the grid sequencing step, the flow computation is carried out first to some reasonable convergence limit at the coarsest grid level and the field values are prolongated (using simple bilinear interpolation) to the next grid level with the grid size equal to half of those at the immediate coarser level. The flow field is smoothed at the finer level for a few iterations and the field values as well as the residues at the fine level are restricted (interpolated) to the immediate coarser level and smoothed to a reasonably low convergence limit. The change of field values at coarse level is then prolongated back to the finer grid level and added to the previous field solution at that fine level. This back and forth computation between two consecutive grid levels using the prolonged fine level residue as source terms at the coarser level constitutes one V cycle. In case of more than two grid levels, the grid-sequencing and V cycle process is carried out in appropriate combination between the coarsest and the finest levels till the pre-decided convergence limit is reached at the finest level.

4 Result and Discussion

The paper discusses five different application examples using the present algorithm. The cicular cylinder is identified as a simple geometry problem with complex flow physics whereas the other examples deal with steady turbulent flow for relatively complex geometry of practical interest.

4.1 Laminar Flow Around Circular Cylinder

The computational domain consists of an annular region between a circle of unit diameter and a square outer boundary of dimension 40 units. The computation domain is divided into 2 blocks consisting of totally 147 nodes along the radial with stretching near the cylinder wall and 206 equally spaced nodes along the circumferential direction. Block 1 forming the left half consists of an inflow boundary at far field , a wall boundary for the half cylinder wall and two cuts separating this block from the neighbouring Block 2 at right as shown in Figure 1(a). An impulsive start of the cylinder is simulated by specifying uniform inflow velocities ($U_1 = 1$ and $U_2 = 0$) in the whole field except at the cylinder wall nodes where no slip conditions are imposed as initial conditions ($t = 0$) and maintained thereafter at all time instants ($t > 0$). Figure 1(b) shows the prescribed boundary condition.

Laminar flow computation is carried out for $Re = 100$ using a timestep of 0.05 units. The phenomenon of alternate vortex shedding is clearly demonstrated by the instantaneous streamlines at three different instants of the shedding cycle(Time Period = T) in Figure 1(c). The temporal variation of the lift and drag coefficients, computed through the integration of the calculated wall pressure and the wall shear stress field, are shown in Figure 1(d). Table 1 shows the present prediction and measurement data of (Norberg, 2001) and those of others adopted from the monograph of (Zdravkovich, 1997) for laminar vortex shedding behind a circular cylinder at $Re = 100$. The computed mean drag coefficient and the amplitude and frequency of the lift coefficient using 2^{nd} order accurate temporal and spatial discretisation scheme are found to be in very close agreement to the measurement data.

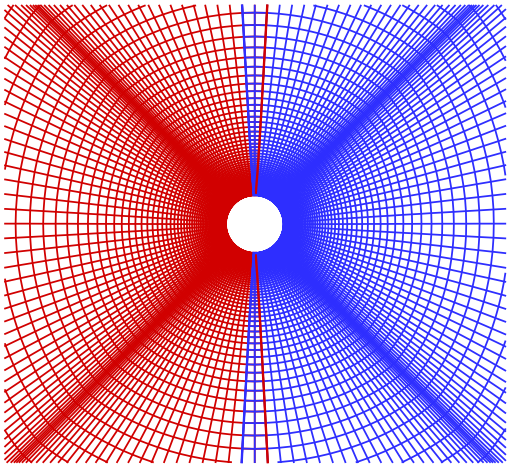

(a) Two block grid near the cylinder wall

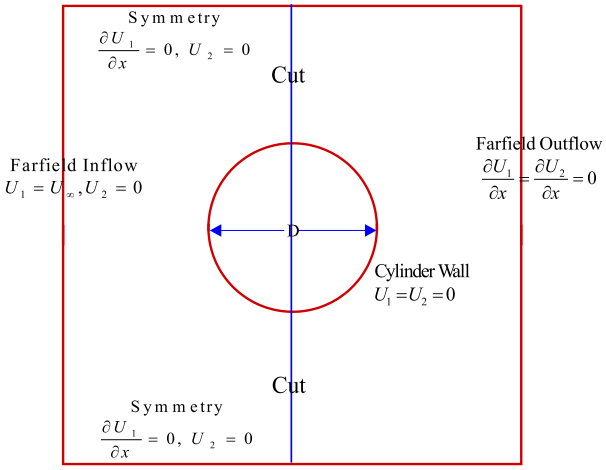

(b) Boundary condition

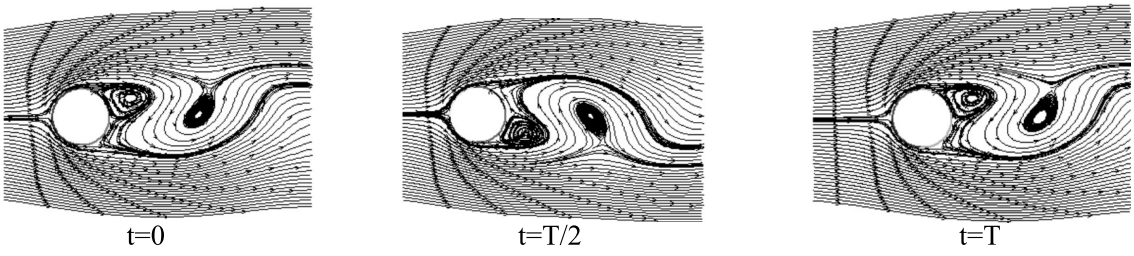

(c) Instantaneous flow pattern

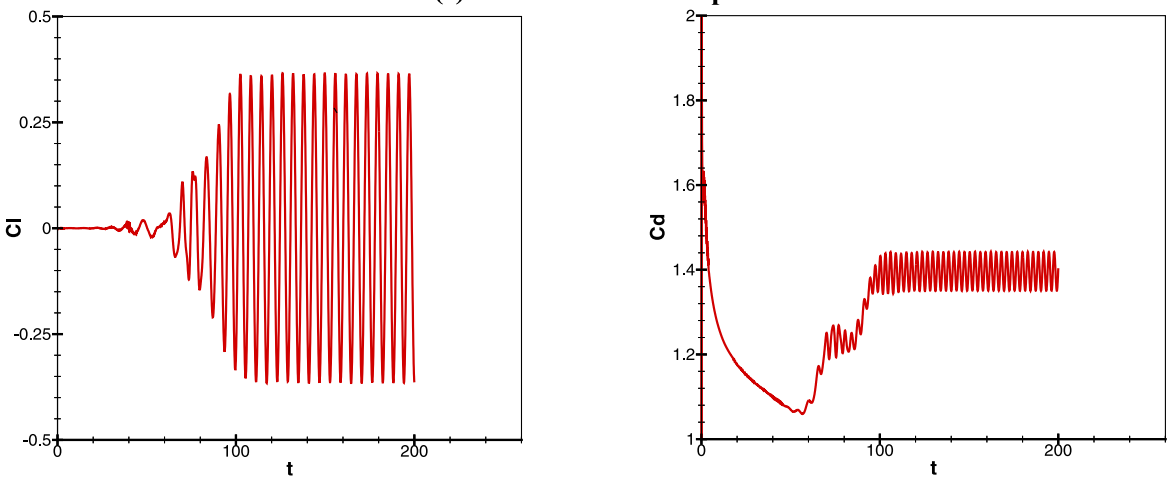

Lift coefficient **Drag coefficient**

(d) Temporal Variation of aerodynamic coefficients

Figure 1: Laminar flow around circular cylinder (Re=100)

Spatial Scheme	Temporal Scheme	Strouhal No. ($St = D/UT$)	C_l(rms)	C_d(avg)
Computation				
Pure Upwind	1^{st} order	0.136	0.102	1.318
HYBRID	1^{st} order	0.137	0.142	1.304
CDS	1^{st} order	0.156	0.232	1.349
CDS	2^{nd} order	0.171	0.283	1.395
Measurement				
Norberg (2000)		0.160	0.25	
Roshko (1953)		0.167		
Tritton(1959)				1.4
Okajima (1973)			0.1	

Table 1: Frequency & amplitude of aerodynamic coefficients for laminar vortex shedding

4.2 Unsteady Laminar Flow Past a Bluff Body Mounted on the Lower Wall of a Plane Channel

This test case is chosen to demonstrate the predictive capability of the algorithm for non-periodic time-dependent flows. In order to study unsteady flow separation on bluff bodies, flow visualization experiments have been conducted (Arakeri, 2002) in a water tunnel at the Mech.Engg. Deptt., IISc, Bangalore using Laser Induced Fluoroscence technique. The experimental set up, reported (Arakeri, 2002) in details, consists of a two-component glass channel filled with water. Water in the top compartment containing the test-body is driven by a piston moved to and fro in the bottom compartment using a controlled servomotor system. The measured velocity-time diagram corresponding to the flow visualization situation is shown in Figure 2(a). Fluorescent Sodium dye is introduced on the body surface and the test plane is illuminated by a 2D Laser sheet. The dye follows the flow pattern and the image on the illuminated plane is captured by a CCD camera at different instants of time during the piston motion. The computation domain is bounded by the horizontal channel top wall, the test body geometry for the channel lower wall, an inflow and outflow plane at a distance of $8H$ on either side, where H = Channel Height. Close view of the H Grid (191×81) near the bluff body, used for computation is shown in Figure 2(b). The uniform inflow velocity condition at different time step is specified according to the linear time-velocity graph of the test condition. The timestep used for computation is $\Delta t = 0.002$ units so that the acceleration period is covered by at least 1000 timesteps. The algorithm uses central difference scheme for convective fluxes and second order time discretisation. Figure 2(c) compares the computed instantaneous streamlines to the flow visualization pictures at three different time instants starting from rest. Reasonably good agreement is obtained between the computation and measurement for the instant and the location of the inception of flow separation. Even at later time instants, the approximate location of the center of the separation bubble in the measured flow image demonstrates reasonably good agreement between measurement and computation for the size and location of the separation bubble growing with time. Some secondary vortices

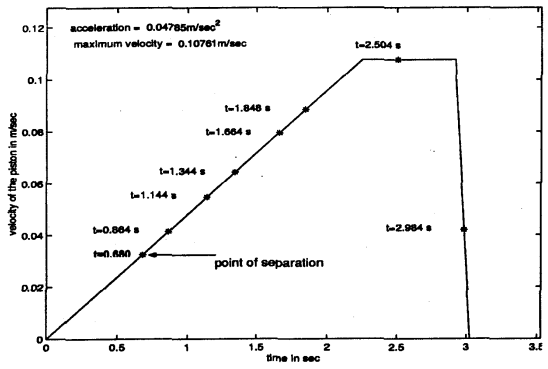

(b) Time-velocity variation in visualization study

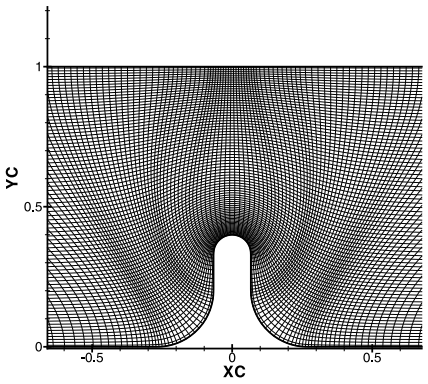

(a) Computational grid

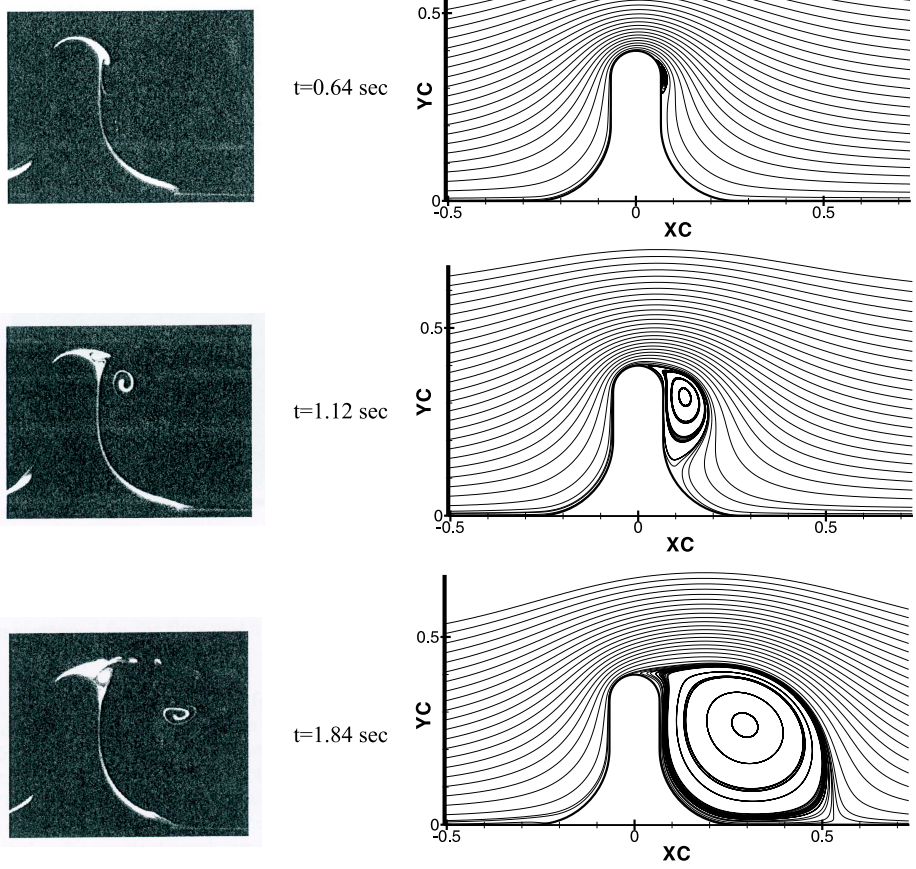

LIF visulization Experiment at IISc [Arakeri, 2002]

Streamlines from unsteady RANS computation

(c) Comparison between computation and flow visualisation experiment

Figure 2: Unsteady laminar flow past a bluff body mounted in a plane channel

observed near the top of the bluff body in the measurement, are however not captured in the present computation. Perhaps a finer near wall resolution of the boundary layer is required to capture these finer near wall structures of the flow more accurately.

4.3 Turbulent Flow Around Circular Cylinder

Turbulent vortex shedding around cylindrical structures is a problem of immense interest in the areas of Offshore Engineering and Marine Hydrodynamics. But for turbulent flow, an accurate prediction depends to a great extent on the choice of the turbulence model and the near wall treatment. Extensive studies have been carried out by the present authors for CFD analysis of this flow at sub-critical Reynolds number ($\mathrm{Re} = 10^5$) using the phase averaged $k - \epsilon$ turbulence model with various kind of near wall treatment and the different spatial and temporal discretisation schemes. This study, sponsored by the Naval Research Board, New Delhi, leads to the conclusion that in the $k - \epsilon$ framework, a low Reynolds number version of $k - \epsilon$ model (Chien, 1982) coupled with the modification (Kato and Launder, 1993) of the stagnation zone, central difference scheme for spatial discretisation and 2nd order temporal discretisation gives the best prediction for the location of separation point and the laminar wall shear stress levels before separation. The grid size and far field boundary location used are same as that for the laminar case (Figure 1(a) & (b)). The computed temporal variation of lift and drag coefficients are shown in Figure 3(a). The summary of the experimental finding and the present computation results using different turbulence models are shown in Table 2 where the computation results using Chien model, Kato modification with fine resolution ($\Delta\theta = 1.8^o$) along the circumferential direction are found to be the closest to the measurement data. Once the computed flow is observed to be statistically stationary, the time averaged value of the flow variables are calculated from 100 consecutive vortex shedding cycles. Figures 3(b) and (c) show the circumferential distribution of the time averaged non dimensional surface pressure (C_p) and the wall shear stress (β) around the cylinder compared to measurement data (Achenbach, 1968). In the pre-separation zone where the boundary layer is practically laminar and the flow is acclerating, the surface pressure with the fine grid resolution is obsereved to be quite close to the measurement data. The maximum skin friction near the the minimum pressure point is however underpredicted and in turn the laminar separation is also delayed in the strongly adverse pressure gradient region. The recovery of pressure in the post separation region does not agree well with the measurement data. The disagreement in surface pressure distribution and the overprediction of the rms lift may perhaps be attributed to the inadequacy of $k - \epsilon$ model for flow in the presence of strong adverse pressure gradient. Perhaps LES or DNS simulations might be more reasonable approaches for resolving such flows with large vortical structures with more than one characteristic frequencies

4.4 Turbulent Flow Around Underwater Body With Appendages

This application example is chosen to demonstrate the capability of the multiblock parallel version of the algorithm for prediction of turbulent flow around axisymmetric bodies with symmetrically placed fins of finite height in the vicinity of the stern end of the hull. The present computation has been carried out for flow around axisymmetric hull of the DARPA Suboff model of submarines with four radial fins fixed at the stern end of the

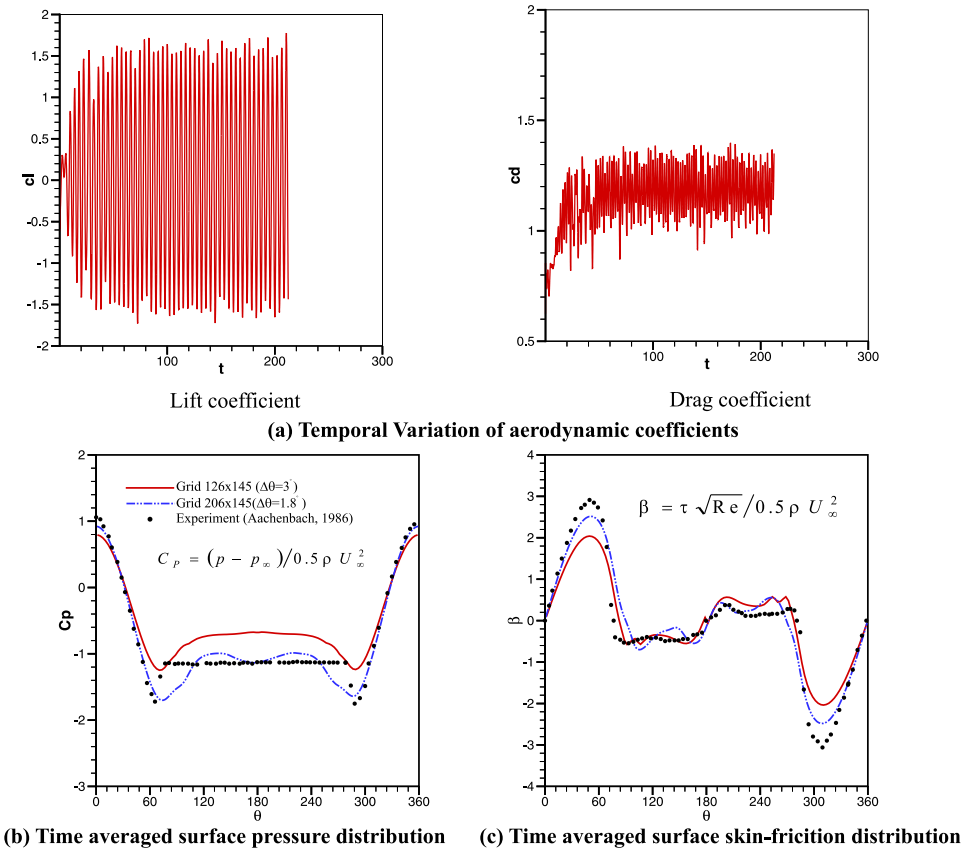

Figure 3: Turbulent flow around circular cylinder ($\mathrm{Re} = 1 \times 10^5$) ($2^{nd}$ order temporal/CDS/$\Delta t = 0.05$ & $k - \epsilon$/Chien/Kato mod.)

		Strouhal No. ($St = D/UT$)	C_l(rms)	C_d(avg)	θ_s
Computation					
$\Delta\theta = 3.0^o$	Std wall	0.238	0.122	0.640	117^o
	Std wall + Kato	0.282	0.281	0.747	105^o
	Chien	0.229	0.091	0.769	81^o
	Chien + Kato	0.204	0.361	0.842	84^o
$\Delta\theta = 1.8^o$	Chien + Kato	0.234	1.000	1.120	90^o
Measurement					
Aachenbach(1968)				1.200	78^o
Norberg(2000)		0.190	0.475		
Bearman(1969)		0.210			
Roshko(1961)		0.275			

Table 2: Aerodynamic coefficients for flow around cylinder for $\mathrm{Re} = 10^5$

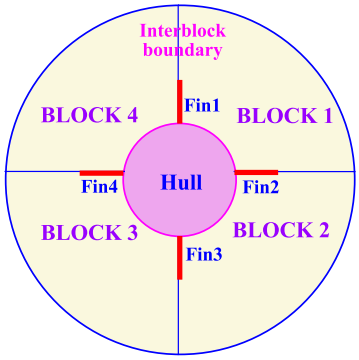

(a) Block arrangement along circumferential (K) direction

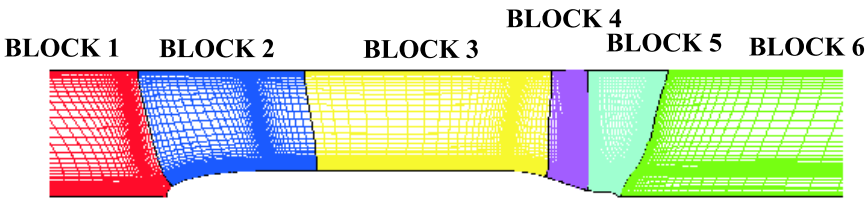

(b) Block arrangement along longitudinal (I) direction

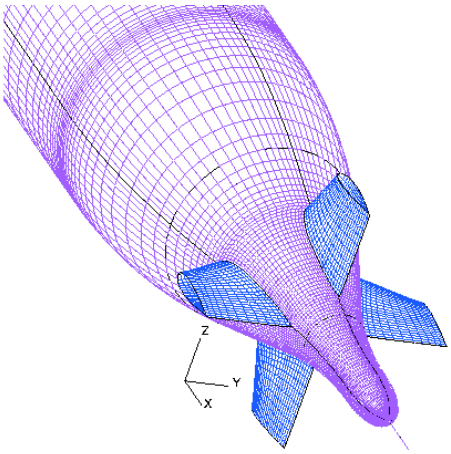

(c) Surface grid near the hull fin junction

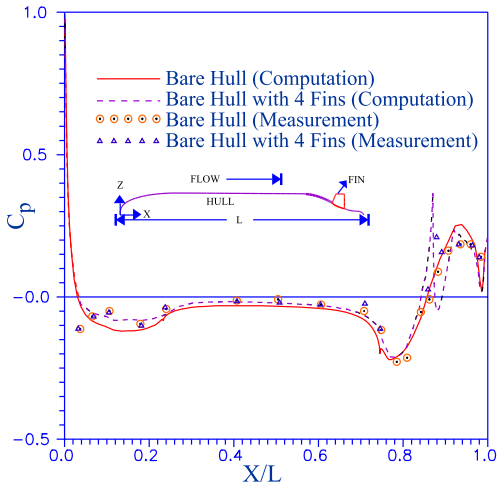

(d) Longitudinal distribution of surface pressure on a vertical meridional plane

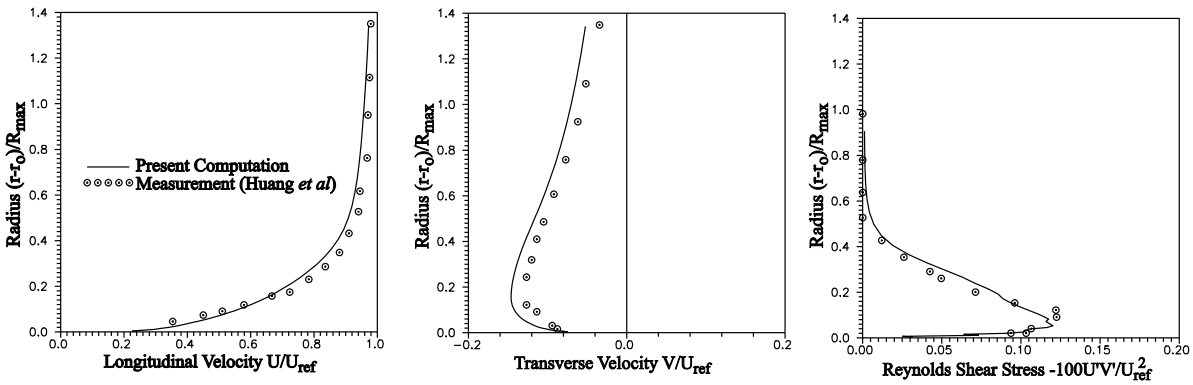

(e) Transverse profiles of mean velocity and Reynolds shear stress

Figure 4: Turbulent flow around a DARPA Suboff body with appendages (Re=1.2×10^7)

Grid: 245x82			
Reynolds Number: 1.2×10^7			
Turbulence Model: $k-\epsilon$, standard wall function			
Multigrid levels: 3			
	Single Grid	Multigrid	Quotient
Iteration	5000(estimated)	255	19.61
Time(min.)	186.65	12.40	15.05

Table 3: Convergence acceleration for 2D computation of flow around underwater body

hull. Detailed hot-film anemometer measurements are reported for this case (Huang et al., 1994) from the David Taylor Model Basin Research Group, USA. A differential-algebraic grid generation procedure developed at the CTFD Division, NAL (Rajani and Majumdar, 1997), is employed to generate structured, boundary-fitted grid required for the present problem. The computational domain is divided into 24 blocks, 4 along the circumferential direction (Figure 4(a)) where each block covers one inter-fin domain, and 6 along the longitudinal direction (Figure 4(b)) depending on the hull geometry. The axisymmetric hull of the body analysed in the present work consists of a forebody, a parallel midbody section followed by an afterbody with four radial fins of NACA0020 aerofoil cross-section attached symmetrically to the hull at four circumferential locations with separation angle of 90^o A H-O grid topology is used with total number of 245 Control Volumes(CV) along longitudinal, 80 CV along radial and 82 CV along tangential directions. A close view of the surface grid near the hull-fin intersection is shown in Figure 4(c). Figure 4(d) compares the measurement data with the present prediction for surface pressure along the vertical meridional plane of the hull with fins. The disagreement between computation and measurement data near the stern end, may be attributed partly to the inaccuracy in the geometry-prescription near the strong curvature zone of the stern end and partly to the well known inadequacy of the $k-\epsilon$ models in the adverse pressure gradient region. Figure 4(e) compares the present prediction to the measurement data for the transverse profiles of the mean velocity component and the Reynolds stress for the bare hull at a longitudinal station $X/L = 0.904$. The agreement is observed to be reasonably good for both mean velocity and the shear component of the turbulent stress. This demonstrates the adequacy of the $k-\epsilon$ turbuelnce model with wall function for attached boundary layer flows.

The same problem has been tried (Mohan and Majumdar, 2002) with the 2D multigrid version of the algorithm with appropriate boundary condition for the vertical meridional plane of the bare hull. Table 3 shows a speed up factor of the order of 15 obtained using a 3 level FAS-FMG procedure for 245×82 grids at the finest level. The flow results obtained are almost identical to the corresponding 3D computation results on the same meridional plane.

4.5 Turbulent Flow Past Aerostat Configuration

Aerostats are large inflated balloons made of strong synthetic fiber kind of material, kept floating in atmosphere at certain height, controlled by tethers attached to the balloon at certain locations and used for surveillance applications. The CFD analysis of the flow

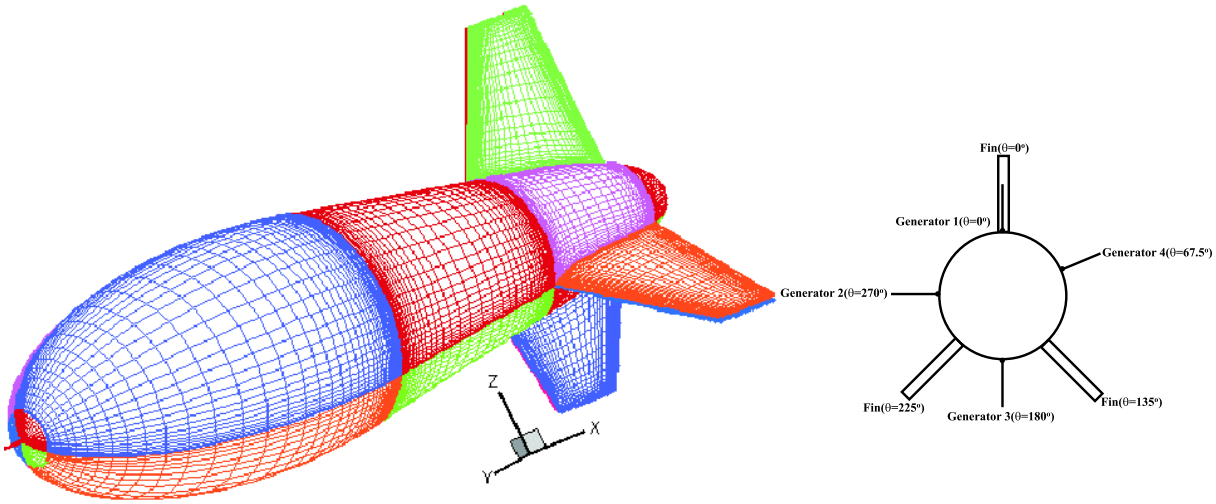

(a) Multiblock surface grid for aerostat

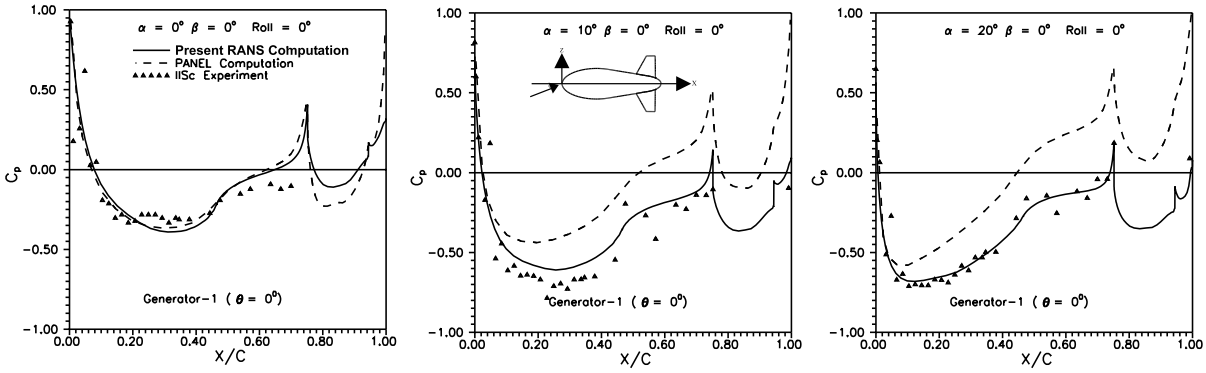

(b) Surface pressure distribution along the top generator of the hull surface

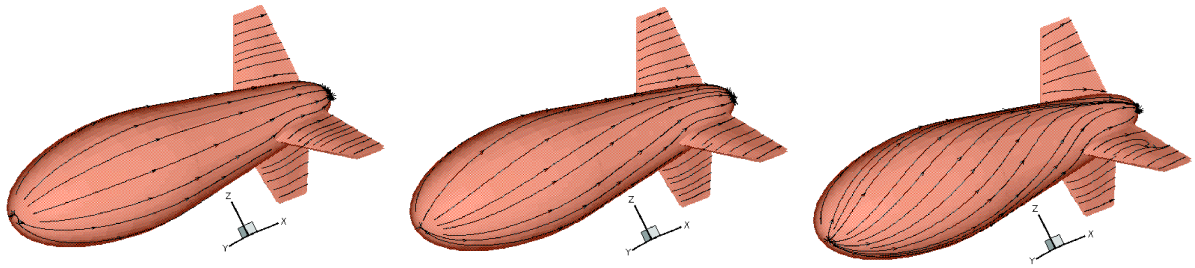

$\alpha = 0^o$, $\beta = 0^o$ $\alpha = 10^o$, $\beta = 0^o$ $\alpha = 20^o$, $\beta = 0^o$

(c) Effect of angle of attack (α) on surface streamlines

Figure 5: Turbulent flow around aerostat (Re=1.5×10^7)

around aerostat configurations ((Majumdar and Rajani, 2001)) has been carried out as a part of an important research project **BLISS** (BaLloon Imaging and Surveillance System) sponsored by the Aerial Delivery Research and Development Establishment (DRDO), Agra. The present aerostat balloon consists of an axisymmetric hull in the form of a body of revolution generated from a smooth aerodynamic shape. Three fins of aerofoil (NACA0018) cross section are attached near the tail end of the hull in the form of an inverted Y in order to enhance the stability of the aerostat under different operating conditions. The computation results obtained by the present RANS algorithm are validated against corresponding Panel code results (Narayana and Srilatha, 2000) and also measurement data obtained from wind tunnel tests carried out on a $1/7^{th}$ scaled model at IISc, Bangalore (Govindraju et al., 1999). For flow analysis of aerostat with finite number of fins, the circumferentially stacked 2D grid is used in the domain outside the fin region. The surface grid on the fins are laid out separately from the given fin geometry and the hull-fin intersection curve is computed accurately using a simple geometry routine. The surface grid on the aerostat with fins is shown in Figure 5(a). QUICK scheme with deferred correction approach and $k-\epsilon$ turbulence model with standard wall function have been used for all the flow computations. The whole computation domain covering $300 \times 82 \times 92$ control volumes (order of 2 million nodes) has been decomposed into eighteen(18) number of blocks computed in parallel using six Pentium processors of NAL Parallel machine Flosolver Mk5, each covering three consecutive blocks along circumferential direction. Figure 5(b) compares the present RANS prediction for the surface pressure data to the corresponding Panel code results and tunnel measurement data from IISc., Bangalore along the top surface generator line of the hull at three different angles of attack (α). The comparison clearly shows much closer agreement of the measurement data to the present RANS solution than to the Panel code results specially for high angles of attack. The computed surface streamlines shown in Figure 5(c) at different angle of attack also indicate physically realistic shift of the stagnation point near the aerostat nose and the consequent bending of the streamlines around the body when α changes from 0^o to 20^o. The discrepancies in RANS prediction for the surfce pressure specially near the tail end may be attributed mainly to the inadaquacy of the $k-\epsilon$ model.

5 Concluding Remarks

The present RANS algorithm for low speed turbulent flow prediction, developed at the CTFD Division, NAL, Bangalore is found to be reasonably accurate for prediction of laminar flows and attached turbulent boundary layers under moderate adverse pressure gradients. For complex flows under the strong effects of curvature or rotation, the agreement between measurement and $k-\epsilon$ prediction is reasonable only in a qualitative sense. The discrepancy in the drag values or even the disagreement obtained in the surfcae pressure or the secondary flow on cross planes for bodies with strong curvature may be attributed mainly to the inherent inadequacy of the $k-\epsilon$ model for adverse pressure gradient zones. Work is in progress to extend the algorithm to a Large Eddy Simulation (LES) procedure and also to incorporate advanced turbulence models, such as the Shear Stress Transport model(Menter, 1992), the Spalart Allamaras (Spalart and Allamaras, 1992) one equation model and the Reynolds Stress transport based $k-\epsilon-v^2-f$ model (Durbin, 1995). Parallelisation of the algorithm is found to be very useful for large

scale computation involved in complex geometry. But the issues of scalability and load balancing however are yet to be optimised.

References

Achenbach, E. (1968). Distribution of local pressure and skin friction around a circular cylinder in cross-flow up to Re=5×10^6. *Journal of Fluid Mechanics*, 34:635–639.

Arakeri, J. H. (2002). Unsteady efffects in hydrodynamics. *Final Report for Naval Research Board Project, Deptt. of Mech. Engg., IISc., Bngalore.*

Chien, K. Y. (1982). Predictions of channel and boundary layer flows with a low Reynolds no. turbulence model. *AIAA Journal*, 20:321–339.

Durbin, P. A. (1995). Separated flows computaion with the $k - \epsilon - \overline{v^2}$ model. *AIAA J*, 33:659–644.

Govindraju, S. P. et al. (1999). Evaluation of aerodynamic forces and moment characteristics on aerostat model in wind tunnel. *Report No. IWTR 273, Deptt. of Aerospace Engg., IISc., Bangalore.*

Huang, T., Liu, H. L., Groves, N., Forlini, T., Blanton, J., and Gowing, S. (1994). Measurements of flows over an axisymmetric body with various appendages in a wind tunnel: the darpa suboff experimental program. *Proceedings* 19^{th} *Symposium on Naval Hydro-dynamics*, National Academy Press:Washington DC.

Kato, M. and Launder, B. E. (1993). The modelling of turbulent flow around stationary and vibrating square cylinder. *Proc. 9th Symposium Turbulent shear flows, Kyoto.*

Khosla, P. K. and Rubin, S. G. (1974). A diagonally dominant secon-order accurate implicit scheme. *Computers and Fluids*, 2:207–209.

Kulkarni, D. S., Rajani, B. N., and Majumdar, S. (July'2001). Studies on temporal and spatial discretisation schemes used in a Pressure-based RANS algorithm for incompressible flow. *NAL PD*, 0108.

Launder, B. E. and Spalding, D. B. (1974). The numerical computation of turbulent flows. *Computer Methods and Applied Mechanics and Engg.*, 3:269.

Leonard, B. P. (1979). A stable and accurate convective modelling procedure based on quadratic interpolation. *Computers Methods in Applied Mechanics and Engg.*, 19:59–98.

Majumdar, S. (1988). Role of underrelaxation in momentum interpolation for calculation of flow with non-staggered grids. *Numerical Heat Transfer*, 13:125–132.

Majumdar, S. and Rajani, B. N. (2001). Numerical computation of flow around aerostats using a pressure-based Navier-Stokes solver. *Journal of Aeronautical Society of India*, 53(2):117–127.

Majumdar, S., Rodi, W., and Zhu, J. (1992). Three dimensional finite volume method for incompressible flows with complex boundaries. *Journal of Fluid Engg.*, ASME:496–503.

Menter, F. R. (1992). Two-equation eddy-viscosity turbulence models for engineering application . *AIAA J*, 32:1598–1605.

Mohan, S. and Majumdar, S. (Dec'2002). Implementation of multigrid in a pressure-based RANS code . *NAL PD*, 0211.

Narayana, C. L. and Srilatha, K. R. (2000). Analysis of aerostat configurations by Panel method. *NAL PD*, 0010.

Norberg, C. (2001). Flow around circular cylinder : aspects of fluctuating lift. *Journal of Fluid Structure*, 15:459–469.

Pal, K., Lalitha, J., Rajani, B. N., and Majumdar, S. (1995). Three dimensional grid generation using elliptic equations with direct control of mesh spacing and orthogonality near boundaries. *NAL PD*, 9511.

Patankar, S. V. (1980). *Numerical heat transfer and fluid flow.* Hemisphere Pub. Co.

Peric, M. (1985). A finite volume method for the prediction of three-dimensional fluid flow in complex ducts. *Ph. D. Thesis, Imperial College, London University.*

Rajani, B. N. and Majumdar, S. (1997). Numerical grid generation around ship hulls using a differential-algebraic hybrid procedure. *Proc. Conf. on Ship and Ocean Technology, IIT Kharapur*, pages 75–80.

Soni, B. K. (1985). Two and three dimensional grid generation for internal flow application. *AIAA Paper*, 85-1526.

Spalart, P. R. and Allamaras, S. R. (1992). A one-equation turbulence model for aerodymanic flow. *AIAA paper*, 92-0439.

Stone, H. L. (1968). Iterative solution of implicit approximations of multidimensional partial differential equations. *SIAM Journal of Numerical Analysis*, 5:530–530.

Zdravkovich, M. (1997). *Flow around circular cylinders: V.1.* Oxford Science Publication.